Additive Manufacturing 78 (2023) 103864

Contents lists available at ScienceDirect

Additive Manufacturing

journal homepage: www.elsevier.com/locate/addma

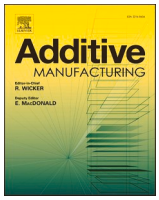

Methodology to predict mechanical properties of PA-12 lattice structures manufactured by powder bed fusion

R. Rodríguez-Aparicio *, J.M. Alegre, W.M.H. Verbeeten, M. Lorenzo-Bañuelos, I.I. Cuesta

Universidad de Burgos. Escuela Politécnica Superior, Av Cantabria s/n, 09006, Burgos, Spain

ARTICLE INFO

Keywords:
PA-12
Selective Laser Sintering
Microstructural defects
Finite Element Analysis
Lattice structure

ABSTRACT

Topology optimization for weight reduction of additive manufacturing parts is commonly achieved throughout the creation of lattice structures, typically generated with beams of small size cross-section. In order to carry out accurate simulations of these lattice structures, knowing the mechanical behavior of pillars is required. In this paper, a methodology for determining the mechanical properties of small size pillars printed in PA-12 material, using polymer powder bed fusion (PBF) and in particular the Selective Laser Sintering (SLS) technology, is presented. The effect of defects originated during the manufacturing process on the macroscopic mechanical properties is studied and the mechanisms which influence these properties are analyzed. A methodology for the determination of these properties is proposed, based on a successive correction of the printed nominal diameters according to two approaches; one due to the outer skin of unmelted material and the other due to internal melting defects. Once the material properties are determined, as a function of the cross-section of the lattice pillars, the numerical simulation of lattice-type structures has been carried out and the degree of adjustment of the proposed methodology has been experimentally verified, obtaining good results. This validation provides a reliable method for the simulation of the macroscopic behavior of lattice-type structures with reduced sizes, taking into account the intrinsic defects generated during the printing process.

1. Introduction

Polymer powder bed fusion (PBF), and specifically the Selective Laser Sintering (SLS) technology, is an additive manufacturing (AM) technique that obtains better mechanical properties than other PBF technologies such as multi jet fusion [1,2]. Nylon 12 (or Polyamide 12) is the polymeric material most widely used in the industry of SLS [3]. This powder material is self-supporting, so no structural support needs to be printed. This technology also allows to recycle the surrounding material of the part that has not been melted [4]. A post-processing step is necessary to remove the poorly sintered powder adhered to the part. Using compressed air still leaves some layers of poorly sintered powder, while using moderately aggressive bead blast could remove it almost completely but slightly modifying the dimensions of the part [5].

This technique of AM enables to develop complex geometries like lattice structures. The unit cell selection of lattice structures can further customize the response of an AM structure (improving mechanical properties, additional lightweighting, thermal properties, and tissue integration). These lattice structures are typically made of cylindrical pillars of small diameter, although any geometry can be adopted for these pillars [6–8]. Moreover, parts with these structures printed with bio-compatible materials can be used for high impact medical applications, enabling complex shapes, high strength parts, and personalized prostheses [9].

To correctly simulate lattices, more complete knowledge of the mechanical properties of different pillar sizes is necessary. The main problem of materials processed with the SLS technology is the high number of defects, lack of fusion (LOF), and the anisotropic mechanical response that considerably affects the mechanical properties of the resulting part [8,10–12]. Moreover, mechanical properties of SLS printed parts are highly affected by printer parameters such as laser power, scan speed, orientation, layer thickness, operating temperature, contouring strategy, beam offset, and powder refresh rate [13,14]. In addition, mechanical properties are also affected by an existing difference between AM bulk and AM lattice. This difference can be explained by the accuracy of the manufacturing technology having a huge impact on small structures reducing mechanical properties [6]. Additionally, AM lattices are usually manufactured with smaller pillars than AM bulk

* Corresponding author.
E-mail address: rraparicio@ubu.es (R. Rodríguez-Aparicio).

https://doi.org/10.1016/j.addma.2023.103864
Received 14 June 2023; Received in revised form 28 October 2023; Accepted 6 November 2023
Available online 8 November 2023

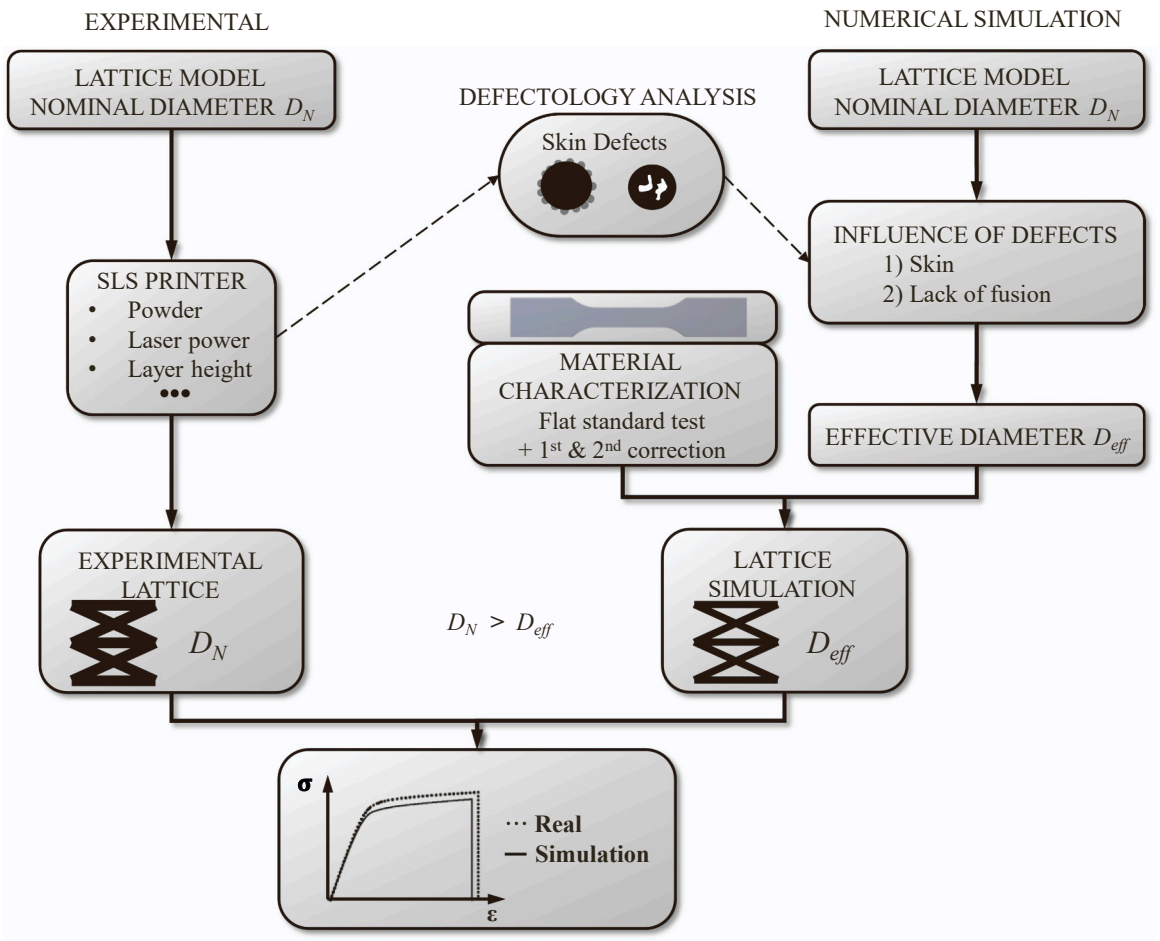

Fig. 1. Methodology scheme to properly simulate SLS printed lattices.

parts. Smaller pillars are subjected to defects of comparable size making them prone to crack in a more brittle fracture than bigger ones. In bigger pillars, defects seem to have a smaller impact on mechanical properties [15]. Furthermore, stress concentration at pillar joints is present in lattice structures which further differentiates the mechanical properties of AM bulk and AM lattice structures [16].

Park et al. [17] analyzed eleven different lattice structures (with different relative densities) using FEM to investigate which structure exhibited higher axial compression yield forces. First, only the unit cell was investigated, followed by research on structures with 2×2×2 and 3×3×3 unit cells. With linear FEM they found the stress concentrates in the connection between pillars. They optimized these zones with a bigger rounding radius, resulting in an increase of compression strength. Tests showed fracture was initiated in these zones. Simple cubic, octahedron, truncated cube, and truncated octahedron lattices exhibited higher axial compression yield forces, indicating better mechanical properties than the other lattice structures studied.

Plocher et al. [18] included the Deshpande-Fleck [19] isotropic model in their FEM analysis modeling the lattices as full blocks with modified properties to mimic the macroscopic ones of the lattices. This non-linear model adjusts approximately the stress-strain curves of the tested lattices, although greater stress is predicted. Moreover, the local stress concentration in the joints of pillars that are prone to crack the lattice were not modeled.

Schob et al. [20] studied in detail the material and introduced the model of Chaboche obtaining a good fitting of the viscous-elastic behavior of PA-12. This model in conjunction with the damage model of Gurson-Tvergaard-Needleman (GTN), previously used in porous metallic materials, could simulate the curve of the material until fracture. The analysis of the microstructure showed a rough surface of the component and an internal porosity. This model can be a good approach to the problem of the present paper but if the studied geometry is reduced (e.g. lattice pillar diameter), this stand-alone mixed model may not be enough.

Smith et al. [21] focused on the lattices behavior under compression, modeling the structures with two types of elements in the FEM analysis. The first were 2-node beam cylindrical elements for the pillars incrementing the diameter near the joints to better capture the geometry. The second were 8-node 3D-brick elements that precisely capture the geometry of the lattice. The non-linear properties of the material were taken from the bibliography and the equivalent diameter of the pillars came from another study [22]. Both elements predicted the initial rigidity, the yield stress and to a lesser extent the plastic zone. Also beam elements failed to model the stress concentration in joints, which were well predicted by 3D-brick elements. It was stated that to obtain better results, a correct estimation of the diameter of pillars is necessary.

Rosso et al. [23] mentioned that a reason for the differences between the experimental and simulated tests is the effect of the size of the lattice pillars. Due to a smaller diameter, the pillars are more prone to fracture because the internal defects and porosity reduce the effective area of the section. Concli et al. [6] studied in aluminum a lattice structure under compression with 2 different diameters obtaining an important different behavior between them. Neff et al. [5] analyzed how reducing the struts thickness of a manufactured diamond lattice changes its stiffness to obtain different mechanical properties using only one material. A study of the cross-section showed lightly sintered layers in the surface. They were measured to correct the nominal dimensions of the struts. Experimental measurements of the stiffness agreed with finite element

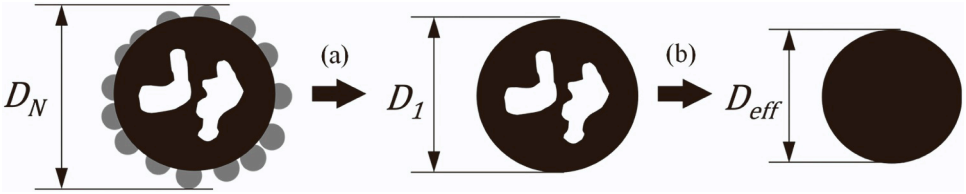

Fig. 2. Diameter corrections to obtain the effective diameter.

simulations after the correction of the thickness and width of the strut, finally, considering only the fully dense region. The thickness of the lightly sintered layers may vary with processing parameters, different machines, and materials.

The present study proposes a methodology focused on determining the mechanical properties of the printed material regardless of the geometry. The main achievement of the study is the creation of a methodology to better reproduce the macro-mechanical behavior in FEM simulations of lattice structures by considering a double diameter reduction of the struts because of the lightly sintered outer layers and internal defects. Material properties obtained by standard tensile tests are corrected and diameter of pillars are reduced to be used in simulations of lattice structures. The proposed diameter reduction is based on SEM fractographies and numerical simulations. Then, simulations are compared to tests of manufactured lattices to validate the methodology.

2. Material and methods

2.1. Methodology

The proposed methodology to determine the mechanical properties of the different pillars as a function of printed diameter and its application to simulate lattice structures is presented in Fig. 1. First, the elastoplastic properties of the base material are studied using standard 1AV specimens under uniaxial tensile tests (from UNE 116005). Then, cylindrical specimens are manufactured by reducing the diameter until the minimum diameter that the printer is able to produce. This is done in order to study both the tensile behavior for different cross sections and the effect of defects on the mechanical properties. An optical and Scanning Electron Microscope (SEM) fractography study on fractured test samples was carried out. This study allows to identify the zones of plastic strain [3], brittle failure, and defects of the material. Subsequently, two consecutive corrections of the nominal diameter are proposed to obtain an effective diameter (Fig. 2): (a) a first reduction of the nominal diameter due to the presence of a non-resistant external layer (i.e. incomplete melting) resulting from the manufacturing technology and (b) a second diameter correction due to the effect of internal defects (LOF) which are a function of the nominal diameter. Finally, some specimens with a lattice structure have been tested and a numerical simulation has been carried out, using the effective diameters, that allows to verify the degree of accuracy of the proposed methodology.

2.2. Material

The material used in this study is a nylon polymer, Nylon 12 (PA-12), a polyamide with a 12-carbon repeating unit. The commercial powder used is from Formlabs Inc. (Somerville, U.S.A.), with a particle diameter between 50 and 90 μm.

2.3. Sample preparation

Specimens and lattice structures were designed with *nTopology* software (version 3.45.4) and then sliced using the printer proprietary software *Preform* from *Formlabs Inc.* (version 3.29.0) in order to manufacture the parts. The dimensions of flat specimens (FS) were adapted from UNE 116005 considering the possibilities of scaling down the

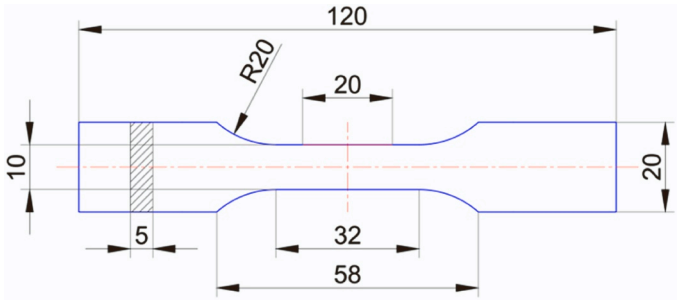

Fig. 3. Dimension of flat tensile test specimens 1AV [mm].

standard dimensions of 1AV tensile specimen (Fig. 3). The thickness of the specimen was 5 *mm* and the cross-sectional area was 50 mm^2. Five specimens were printed for each orientation (vertical {V} and horizontal {H}), as is shown in Fig. 4.

For manufacturing flat, cylindrical and lattice specimens the printer *FUSE 1* was used, with SLS technology from *Formlabs Inc*. The laser is made of ytterbium fiber with 10 *W* of power (with a wavelength ten times smaller than usual CO_2 lasers), a laser scan speed of 6 *m/s*, layer thickness of 110 μm, and an operation temperature of 180 °C.

For cylindrical specimens (CS), dimensions corresponding to Specimen 4 of ASTM E8M standard have been adopted, by varying the nominal diameter of the specimen from 8 *mm* (approximately the same cross section as the flat specimens) to 1 *mm*, through 4 *mm* and 2 *mm* (Fig. 5). In this case, for each diameter 3 specimens were manufactured in the horizontal {H} orientation.

The dimensions of lattice specimens (Fig. 6) were defined, such that they could fit correctly between the cross-head clamps of the universal test system. Specimens had a width of 25 *mm* and a 7 *mm* thickness. For an adequate grip of the specimens, grip zones of 30 *mm* length were chosen (see Fig. 6). The lattice structure has a 60 *mm* length, which is the initial distance between grips.

The lattices (Fig. 7) were created with the *nTopology* software using patterns of the "Octet", FCC or "Face Centered Cubic", and BCC or "Body Centered Cubic" type. These types of lattices were selected to prove the methodology, because they are commonly used in topology optimization of components. The nominal diameter D_N of the pillars for printing was 2 *mm*. This diameter was selected because it was small enough to create a lattice with several pillars that still fit in the testing machine. Two flat specimens of each pattern were manufactured horizontally {H}.

After printing, all standard specimens and lattices were cleaned with compressed air and then stored inside a glass desiccator in dry conditions and room temperature.

2.4. Mechanical characterization

Tests were carried out on a MTS-Criterion C43.104 universal test system equipped with a 10 *kN* load cell. A laser extensometer Epsilon LE-05 was used, measure range between 8 and 127 *mm*, resolution of 0.01 *mm*, linearity of ± 0.01 *mm* and repeatability of ± 0.005 *mm*.

For tensile tests, the UNE-EN ISO 527–2:2012 standard specifies a nominal strain rate between crossheads of $\dot{\varepsilon} = 1\%\ min^{-1}$. The initial distance in flat specimens between crossheads was 85 *mm* in compliance

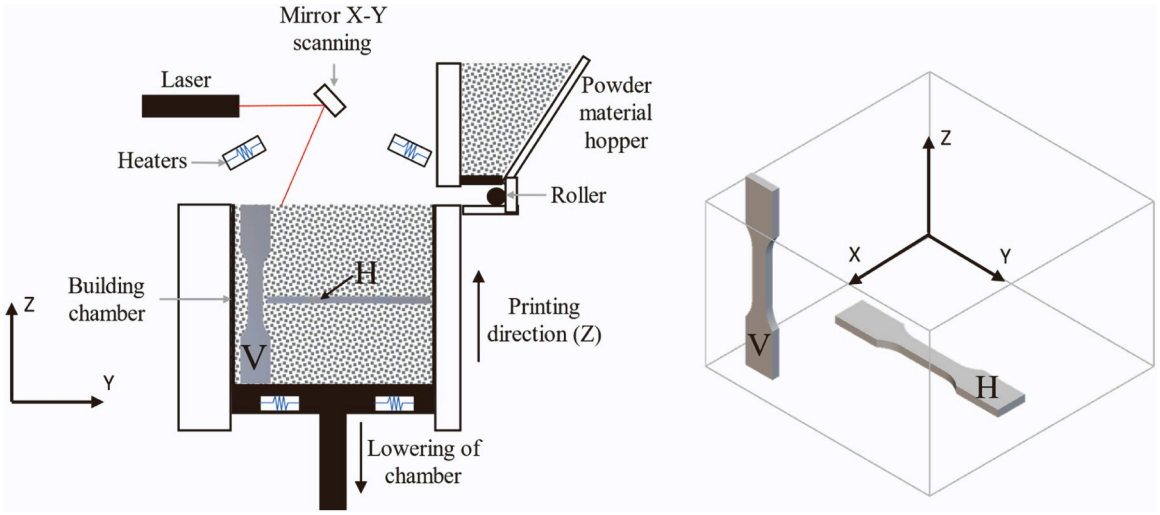

Fig. 4. Working scheme of SLS technology of Fuse 1 printer from Formlabs, and specimens orientation.

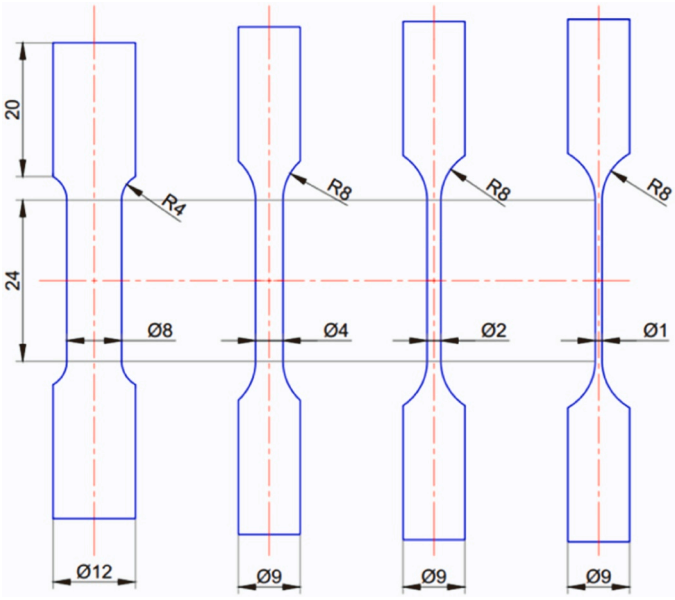

Fig. 5. Cylindrical specimens (CS) geometry and dimensions [mm].

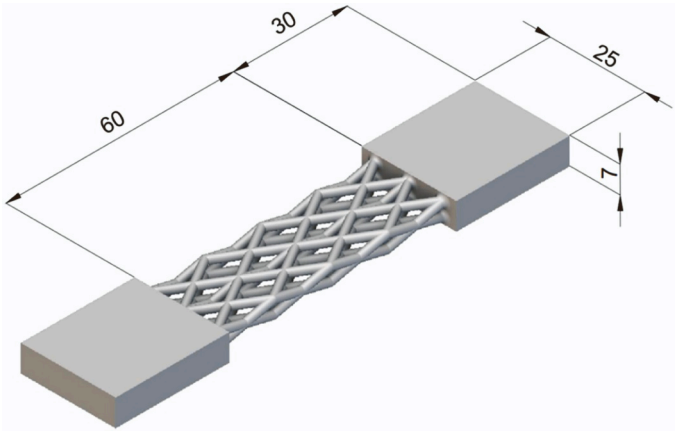

Fig. 6. Lattice specimen dimensions [mm].

with the standard. Accordingly, the crosshead speed was set to 0.85 *mm/min*, following the next equation (Eq. 1):

$$\dot{\varepsilon} = \frac{C_m}{L}, \tag{1}$$

where, C_m is the crosshead speed and L the initial length between crossheads.

As the objective of this study is to compare the results with the flat specimens, the same nominal strain rate ($\dot{\varepsilon} = 1\%\ min^{-1}$) was chosen for cylindrical specimens. For CS specimens, the initial distance between crossheads is 45 *mm*, obtaining a crosshead speed of 0.45 *mm/min*. For lattice specimens, the chosen crosshead speed is 0.60 *mm/min* in order to maintain the same nominal strain rate along the study.

To identify correctly all the specimens a nomenclature is designed. For flat specimens, the first letter indicates the orientation (H, horizontal and V, vertical), followed by a number which means the number of the test and, finally, the word "*FLAT*" that refers to a standard specimen, (e.g. H1_FLAT). In the case of cylindrical specimens, the nomenclature consists of a first letter which indicates the orientation, followed by a number referring to the nominal diameter of the specimen, and, last, the number of the test and the word "*CYL*" which indicates a cylindrical specimen (e.g. H8_2_CYL, horizontal 8 *mm* diameter - specimen number 2 - cylindrical specimen). For lattice specimens an easy nomenclature is designed consisting of, first, the name of the pattern (octet, BCC or FCC) and then the number of the specimen (e.g. BCC-01).

2.5. Optical and SEM fractography

To optically analyze the fracture surface of the specimens, an S9i Stereozoom model from Leica Microsystems (Switzerland) Ltd. with 5.5 magnifications has been used connected to a computer. For capturing and processing images Leica Application Suite software (version 4.12.0) was used.

In the case of SEM fractography, a Jeol JSM-6460LV with 20 kV configuration was used. An Emitech 500 system was applied to coat the PA-12 specimens with gold (Au).

2.6. Simulations

All simulations carried out have been done in the environment of the software Ansys APDL (version 2023 R1). It should be noted that in this paper, only the behavior of the printed material in H direction (Fig. 4) has been considered to model the material in the simulation. The orientation of the pillars in the horizontal plane is not affected by the

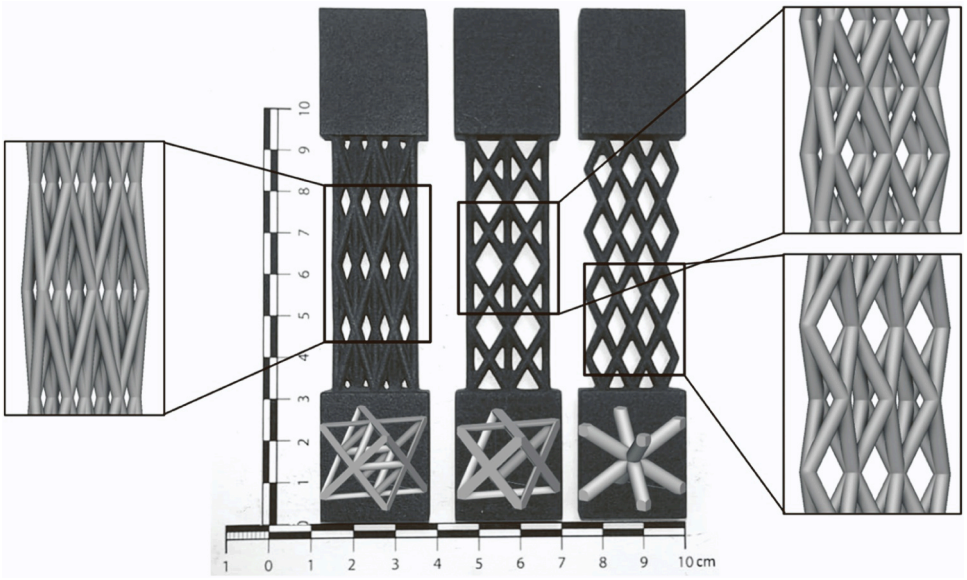

Fig. 7. (Left to right) Octet, FCC, BCC. Image of frontal plane, 3D close up of each geometry and reference unit cell below each specimen.

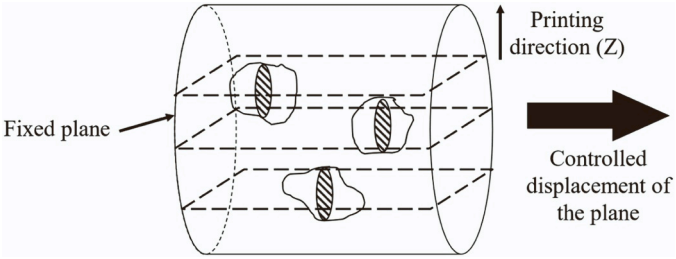

Fig. 8. Base geometry for defects numerical simulation.

anisotropy of the material, since it is assumed that it is a transversely isotropic material (the anisotropy is only presented in the V direction, i.e. the direction of the layers deposition). So, this is a correct approach to simulate lattice structures under uniaxial tensile tests printed in the H direction. The evaluation of material anisotropy is out of the scope of the present paper. From standard tensile tests, an experimental stress-strain curve of the material has been obtained and then used as input for the material data of the simulations. As PA-12 has a viscous-elastic-plastic behavior, 8 points of the experimental curve are selected and introduced in Ansys APDL via the "multilinear isotropic hardening plasticity" option.

2.7. Porosity estimation

To understand the effect of porosity (Φ) on the experimental stress-strain tensile curve, a numerical simulation of the tensile tests including defects (internal non-meshed zones) (Fig. 8) was used.

As an example, for the 1 *mm* diameter cylindrical specimen, a cylinder of 1 *mm* length is modeled considering the skin width of 144 μm (resulting from the first correction) to be subtracted from the nominal diameter. The modeled defects and pores are parametrized as an equivalent cylindrical defect giving rise to the same volumetric porosity. The number of these defects and the distance separating them are also parametrized to achieve a random distribution in the material.

For implementing the material behavior of PA-12 in ANSYS, the average experimental curve for a horizontal flat specimen with the first correction (elimination of the skin and reducing cross section) is chosen. The elements for meshing the geometry are second order tetrahedra (10 nodes) with an element size of 0.05 *mm*. The displacement of one of the

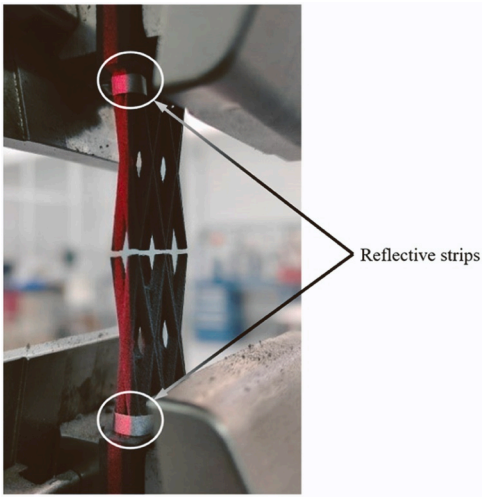

Fig. 9. Tensile test failure for Octet lattice specimen.

bases of the cylinder is restricted, but the contraction of the specimen is allowed. The displacement of the other base is set as a loading condition. This displacement is done in 15 steps with linear increment and the average stress on the upper face is taken.

2.8. Lattice specimen simulation

The material behavior used is the average behavior of a horizontal flat specimen including both corrections. The nominal diameter sent to the printer is 2 *mm*. However, for the simulation, a first correction is applied to this initial diameter, which consists of reducing the diameter with twice the thickness of the skin (2·0.144 *mm*, obtained from the results of the first correction) and a second correction is applied to the resulting diameter (1.712 *mm*) due to the porosity of the process (considered to be 5.50% as detailed in Section 3.1.4). The final diameter used in the simulation was 1.66 *mm*. At first glance, it seems to be that the corrections are applied twice. However, by taking the average corrected curve of the horizontal flat specimen, the behavior of the pure material is introduced. Then, by reducing the diameter of the lattice pillars, they are converted to a diameter that would result if the printing

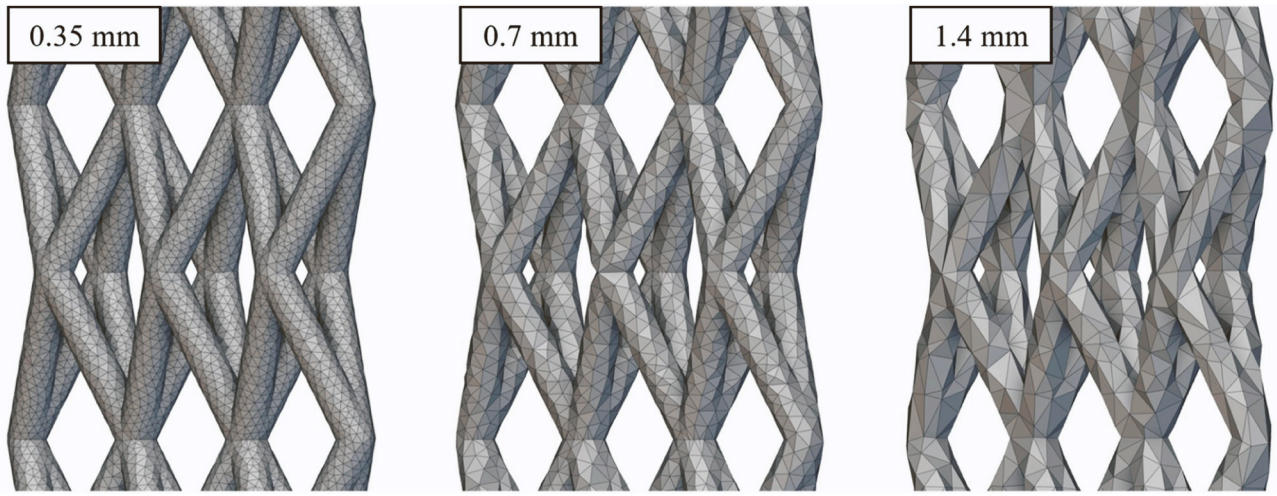

Fig. 10. BCC specimen meshed with different element size for a convergence analysis.

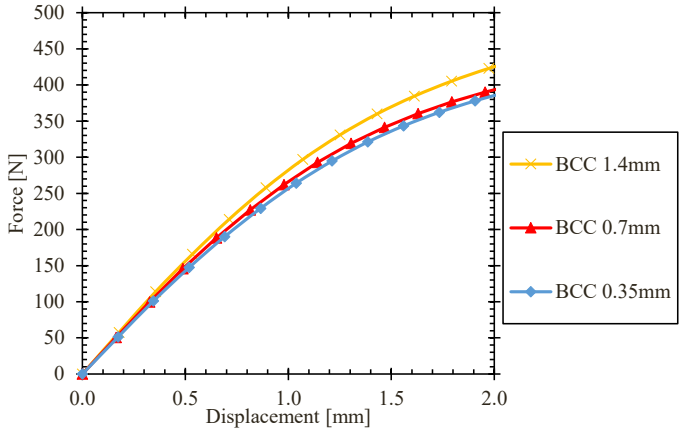

Fig. 11. Load-displacement curves as a function of element size.

process did not leave any outer skin or internal defects.

A new lattice is created with this final diameter but maintaining the unit cell, so the shape is exactly the same but with a corrected effective diameter. The volume mesh of the new lattice is created with second order tetrahedra (10 nodes) elements with an edge length of 0.7 *mm* (resulting from the convergence analysis). The analysis has been divided into 15 steps and the distance between two nodes has been monitored, simulating the real case in which displacement is measured by laser extensometer between reflective strips at the ends of the lattice (Fig. 9). To be as close as possible to the real test, reaction forces have been obtained on the surface that is constrained to move.

2.9. Mesh discretization and convergence analysis for lattice simulation

The elements for meshing all the lattices are second order tetrahedra (10 nodes). Mesh convergence studies were performed on the full BCC specimen to determine when the quantities of interest (QOI) are sufficiently mesh independent. Only one kind of the three lattice specimens was tested because all specimens have the same pillar diameter. The control of the axial displacement of the bases is set as a loading condition. This displacement is done in 15 steps with linear increments. This time the input material for ANSYS is the same experimental stress-strain curve as before but with the second correction applied. Element sizes varied between 1.40 and 0.35 *mm* (Fig. 10). The reaction force at the constrained faces is recorded to plot the simulated load-displacement curves using different element sizes (Fig. 11). Maximum stress given by Von Mises and the reaction forces were also recorded at an equivalent 2 *mm* displacement. Results are shown in Table 1.

Table 1
Mesh convergence results for BCC lattice specimen. % difference is related to the preceding larger element.

Element size	Force [N]	% Difference	Max. Von Misses stress	% Difference
1.40	425.06	–	61.10	–
0.70	393.32	8.07	61.89	0.99
0.35	385.16	2.12	61.74	1.00

From the convergence analysis results, a 0.70 *mm* element size was proven sufficient to proceed because the mesh refinement acceptance criteria were met. This criterion was based on the convergence of the QOI within 5% with a halving of element sizes. When halving the element size from 0.70 to 0.35 *mm*, both QOI (force and maximum Von Misses) remained below the 5% as can be seen in Table 1.

3. Results and discussion

3.1. Mechanical properties

3.1.1. Standard material characterization

Stress-strain curves (Fig. 16) are obtained for flat and cylindrical tensile specimens with different cross section and the same nominal

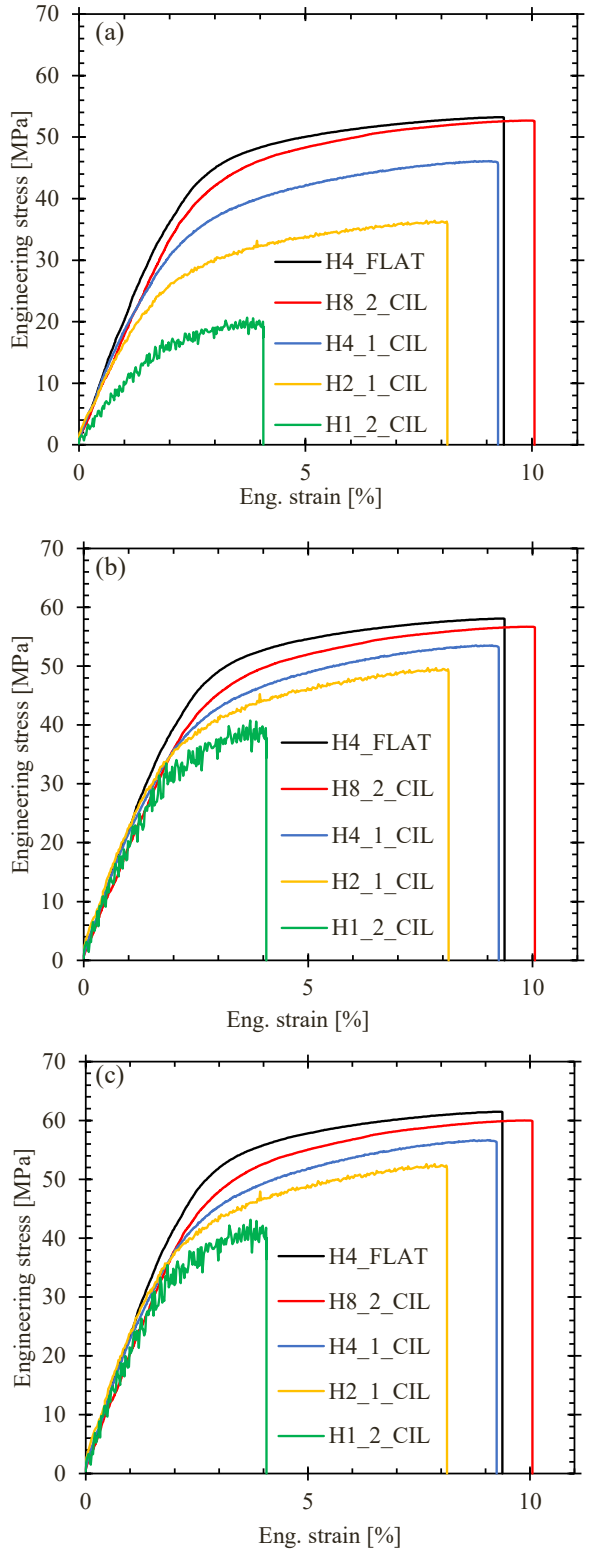

Fig. 16. Representative engineering stress-strain curves of each size, (a) No correction (b) First correction (c) Second correction.

strain rate $\dot{\varepsilon} = 1\%min^{-1}$. Table 2 and Table 3 collect the Young's modulus (E), ultimate tensile strength (σ_{UTS}), and elongation at break (ε_{max}) obtained from the previous experimental curves.

Fig. 16 (a) shows a representative stress-strain curve of flat specimen and cylindrical specimens with 8, 4, 2 and 1 *mm* in diameter, respectively. As observed in Table 2 and Table 3, despite being the same material only changing the specimen cross section, a wide disparity of mechanical properties is detected not linked to the experimental dispersion. Consequently, they cannot be used as input for numerical simulations, so a deeper study of the material properties as a function of the printed diameter is necessary.

Table 2
Mechanical properties of flat standard specimens.

Orientation	H	V
E [MPa]	2152 ± 109	1922 ± 191
σ_{UTS} [MPa]	53.3 ± 0.4	42.8 ± 0.7
ε_{max} [%]	8.5 ± 0.8	4.2 ± 0.3

Table 3
Mechanical properties of horizontal cylindrical specimens.

Diameter [*mm*]	H8	H4	H2	H1
E [MPa]	2054 ± 253	1698 ± 154	1484 ± 116	954 ± 78
σ_{UTS} [MPa]	52.9 ± 0.2	45.9 ± 0.6	34.6 ± 1.6	20.7 ± 0.3
ε_{max} [%]	9.5 ± 1.0	9.5 ± 0.3	7.5 ± 0.7	4.2 ± 0.6

3.1.2. Failure mechanism observations

To better understand the different behavior in specimens of the same material and different geometry, an analysis of the fracture surface of the tensile tests has been done. Fracture surface appearance of the specimens, analyzed using optical microscopy, are shown in Fig. 12. In order to analyze the failure mechanisms and their effect on the mechanical properties, SEM fractography is also used (Fig. 13).

On flat specimens (Fig. 12a and Fig. 12b), whitish zones around the edge of the section can be observed, corresponding to poorly fused material due to the manufacturing technology. This effect can be justified by the printing process: Initially the laser fuses the first layer causing an adhesion of the surrounding powder. Then, a second powder layer is added and slightly adhered to the first zone already fused. This time, the laser fuses powder above an already fused material causing a better adhesion between layers. The process continues with good adhesion between layers until printing of the last layer or the outer zones of the part, which fuses to the previous one, but the powder deposited afterwards will adhere to the piece without fusing completely, giving rise to an outer layer with poor resistance properties, that will be termed here as skin (Fig. 14).

On cylindrical specimens (Fig. 12c), the outer skin surrounding the cross section is clearly observed. The SEM fractography shows two main distinct zones (Fig. 13b). In tension, the region of the cross-section with high local stresses produces so-called crazing [24] (Fig. 13c). This mechanism begins from a LOF defect with the formation of small and interconnected microvoids. These gap connections elongate with increasing stress and when they break, produce a fibrous aspect. This phenomenon is a result of the fracture toughness of the material due to its ability to absorb energy before breaking, usually accompanied by a whitening of the area. And finally, a brittle fracture aspect is observed at the final failure (Fig. 13a). Internal defects are seen in all analyzed fractography images. The failure of the specimens occurs in the layer where the larger defect is encountered, reducing the effective cross section and the force it can withstand. This has to be taken into account when performing simulations.

3.1.3. First correction of skin

In Fig. 12 and Fig. 13 a deficient fusion on the outer layers is shown both on flat and cylindrical specimens. This external layer exhibits reduced mechanical properties compared to the entire part.

Consequently, the first proposed correction consists of disregarding this skin of the cross-section, considering a decrease in the effective diameter of the specimen that will affect the calculation of the tensile stress for a given load applied in the tensile tests. The size of this skin has

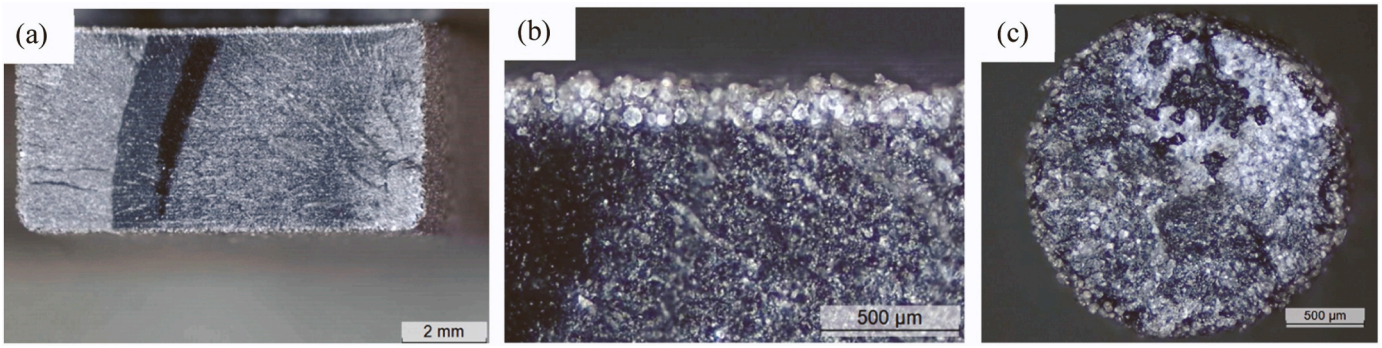

Fig. 12. Optical micrography of specimens: (a) FS section, (b) FS edge, and (c) CS section.

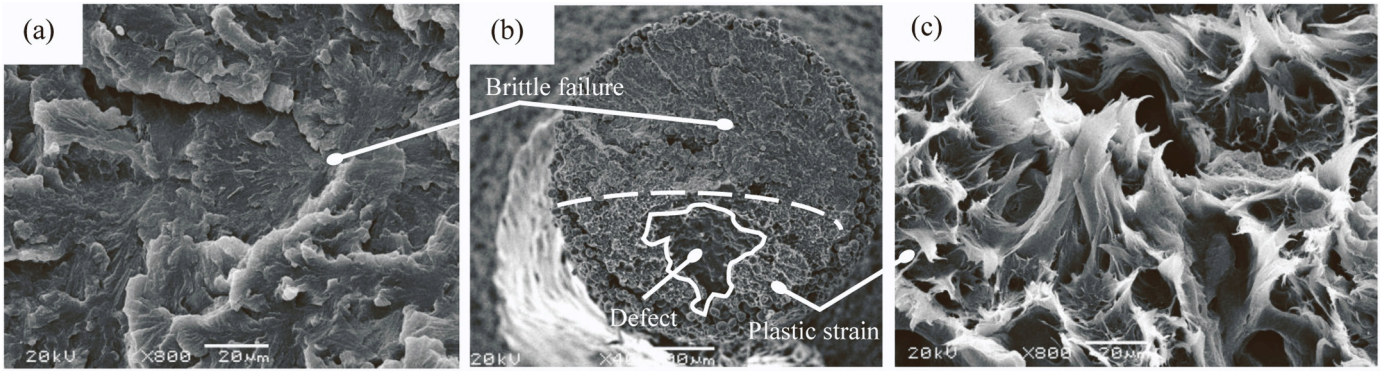

Fig. 13. SEM microscopy of 2 *mm* horizontal CS: (a) brittle failure, (b) section, and (c) plastic strain.

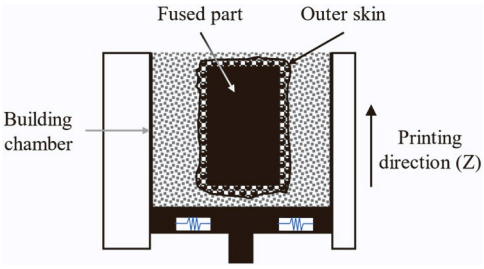

Fig. 14. Scheme of fused part and outer skin.

been measured through optical microscopy image analysis obtaining an average value of $c_1 = 144 \pm 14\ \mu m$.

For FS the new cross-section is the original dimension measured (D) with vernier caliper minus twice the skin (Eq. 2). For CS the nominal diameter minus twice the skin is taken (Eq. 3). (Nominal diameter is adopted as the average since measures of specimens were as close as $\pm$ 0.01 *mm* to the nominal diameter)

$$A_{0,flat} = b \cdot h \rightarrow A_{1,flat} = (b - 2c_1) \cdot (h - 2c_1) \tag{2}$$

$$A_{0,cil} = \frac{\pi D_N^{\,2}}{4} \rightarrow A_{1,cil} = \frac{\pi (D_N - 2c_1)^2}{4} \tag{3}$$

To obtain the tensile curves of PA-12, the effective cross-section is taken as the one after applying the first correction. Fig. 16 (b) shows the representative stress-strain curves after the first correction due to the non-fused material skin. The initial zone, responsible for the elastic modulus of the material, does now coincide for all samples.

3.1.4. Second correction of pores and defects

Despite the improvement for the initial part of the stress-strain curves after the first correction (Fig. 16 (b)), a clear reduction of the plastic properties and deformation capacity with the printing diameter is still observed. This reduction is attributed to the presence of internal defects due to LOF, mainly located between layers, which greatly affect the engineering tensile stress-strain curves (Fig. 16 (a) and (b)). These LOF defects are more critical in thinner specimens. Consequently, a second correction based on a FEM analysis of the internal defects is proposed to adjust the stress-strain curves.

Fig. 15 shows the degree of fit of the material behavior between the experimental tensile test and the simulation of the reference material with different sized defects. By means of an iterative process, it is obtained that a porosity (Φ) of 5.51% adequately adjusts the corrected experimental curves (without the skin) for the 1 *mm* nominal diameter specimen. A similar porosity is obtained for the rest of the configurations, concluding that approximately 5.50% of the volume of this material are internal pores or defects.

Therefore, the second corrected diameter or the effective diameter (D_{eff}) is obtained from the second corrected volume (V_2) to the once corrected volume (V_1) minus the pore volume (V_{def}) (Eq 4). These defects result in an equivalent diametral reduction, according to:

$$V_2 = V_1 - V_{def} \tag{4}$$

$$h \cdot \frac{\pi D_{eff}^{\,2}}{4} = h \cdot \frac{\pi D_1^{\,2}}{4} - \frac{\pi D_{def}^{\,2}}{4} \cdot h_{\,def} \cdot n^{o}_{def} \tag{5}$$

$$\frac{h \cdot \frac{\pi D_{eff}^{\,2}}{4}}{h \cdot \frac{\pi D_1^{\,2}}{4}} = \frac{h \cdot \frac{\pi D_1^{\,2}}{4}}{h \cdot \frac{\pi D_1^{\,2}}{4}} - \frac{\frac{\pi D_{def}^{\,2}}{4} \cdot h_{def} \cdot n^{o}_{def}}{h \cdot \frac{\pi D_1^{\,2}}{4}} \tag{6}$$

$$\frac{D_{eff}^{\,2}}{D_1^{\,2}} = 1 - \Phi \tag{7}$$

Where h_{def} is the height of the defect, n^{o}_{def} the number of defects in the simulation, D_{def} the defect diameter, and h the length of the cylinder in

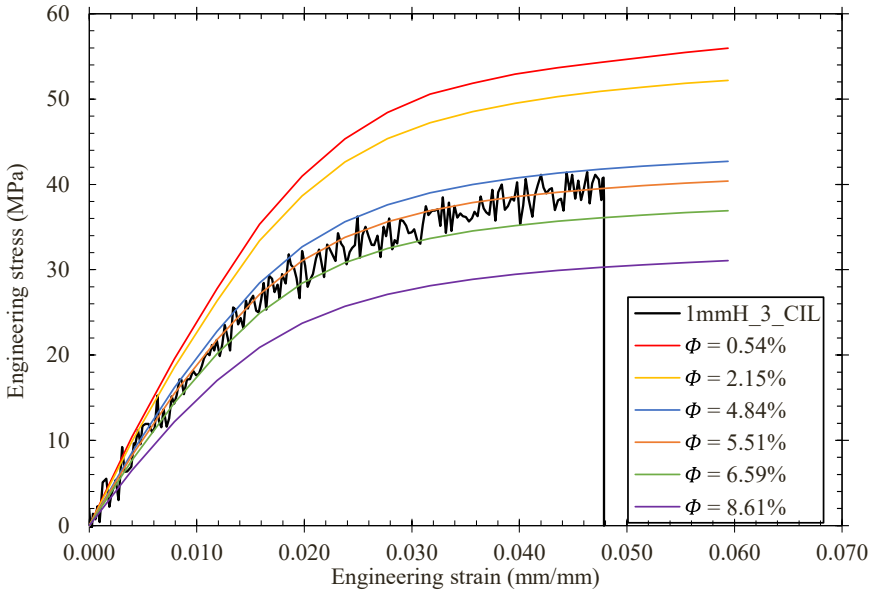

Fig. 15. Real curves of 1 *mm* in comparison with simulated porosity.

Table 4
Corrected properties of flat specimens.

Orientation	H	V
E [MPa]	2486 ± 128	2221 ± 221
σ_{UTS} [MPa]	61.6 ± 0.5	49.5 ± 0.8
ε_{max} [%]	8.5 ± 0.8	4.2 ± 0.3

Table 5
Corrected properties of horizontal cylindrical specimens.

Orientation	H8	H4	H2	H1
E [MPa]	2339 ± 288	2087 ± 189	2144 ± 168	1992 ± 163
σ_{UTS} [MPa]	60.3 ± 0.2	56.4 ± 0.7	50.0 ± 2.3	43.2 ± 0.7
ε_{max} [%]	9.5 ± 1.0	9.5 ± 0.3	7.5 ± 0.7	4.2 ± 0.6

the simulation (see also Fig. 8).

3.1.5. Corrected mechanical properties

The mechanical properties from the tensile tests after the second correction are presented in Table 4 and Table 5. The maximum strain is decreased by reducing the diameter of the pillars of the specimens. From the second correction a practically constant Young`s modulus is obtained although the diameter of cylindrical specimens is varied (Fig. 17). σ_{UTS} has increased after the corrections, but the value diminishes with decreasing diameter (Fig. 18). In Fig. 16, the representative stress-strain curves of all the specimens are shown, which include the second correction. After the first correction the elastic zone coincides for all the specimens. Then, the second correction improves the mechanical properties, i.e. the elastic modulus and the ultimate tensile strength, of all the studied specimens.

3.2. Lattice structure simulation

For the three different lattice specimens, a comparison has been made between the simulated reaction force due to the constrained displacement and the experimental tensile test (Fig. 19, Fig. 20, and Fig. 21). From the simulation, the maximum Von Mises equivalent stress in each of the steps has also been obtained to compare with the material behavior because a fracture model based on σ_{UTS} has been used.

There is a good experimental repetition. The simulations describe

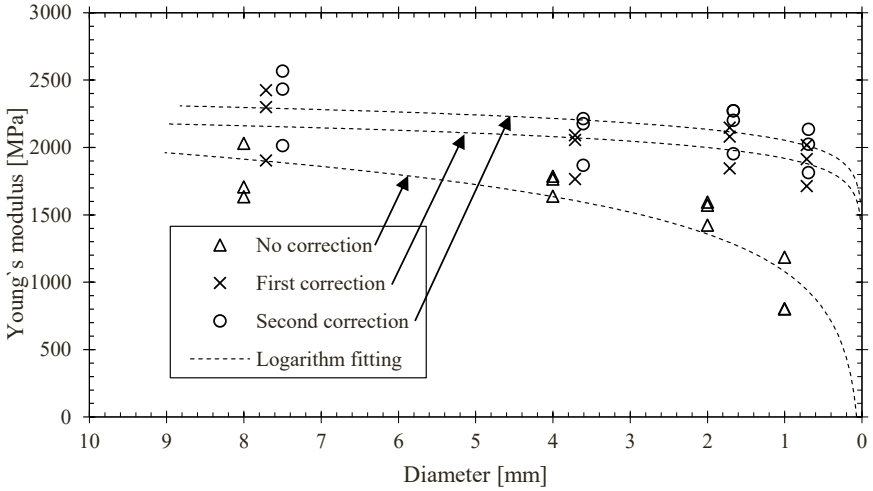

Fig. 17. Young`s modulus comparison between corrections and diameters.

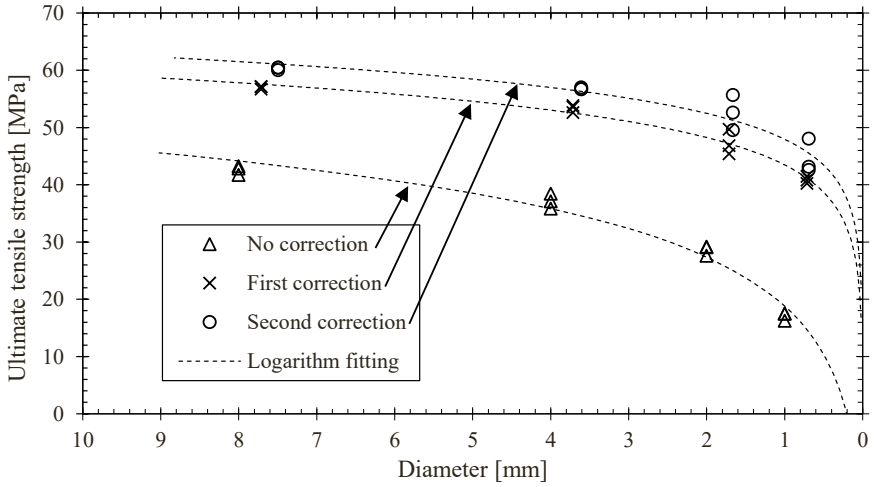

Fig. 18. σ_{UTS} strength comparison between corrections and diameters.

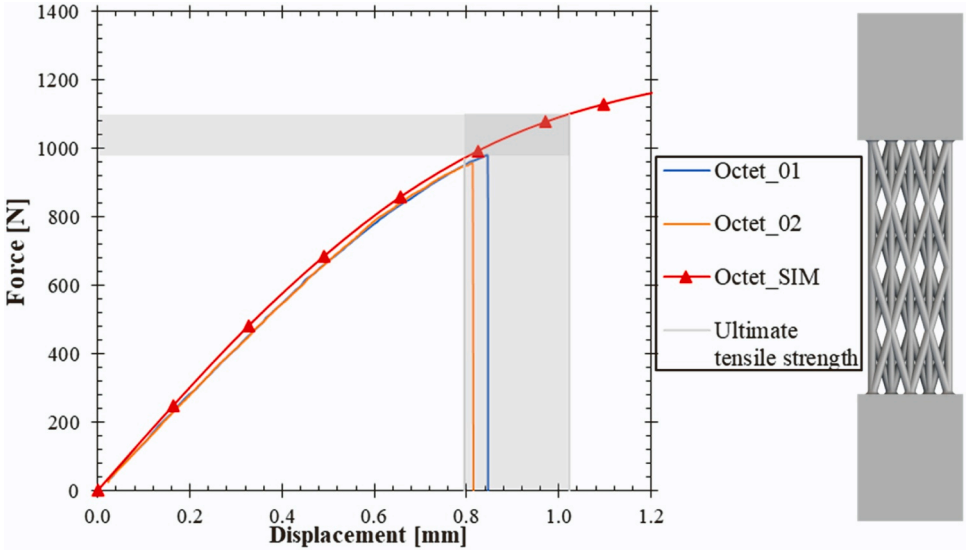

Fig. 19. Octet comparison between simulation with fracture limits and tests.

remarkably well the force-displacement curve of the experimental tensile tests. The shaded area is the σ_{UTS} range of PA-12 ($\sigma_{UTS} = 61.6 \pm 0.5 MPa$), as determined from the corrected tensile test characterization (see Table 4). In the "Octet" type lattice (Fig. 19) the experimental failure is inside the expected range of the fracture model of the simulation based on the ultimate stress. For the "BCC" lattice (Fig. 21) the simulation also fits the real test force-displacement curve and the point of failure. For the "FCC" lattice (Fig. 20), the simulated displacement of failure is slightly lower than the experimental one, although the failure force value is correctly predicted.

The simulations give a good result compared to the force-displacement curve of the tensile tests performed (see Fig. 19, Fig. 20, and Fig. 21). Maximum Von-Mises equivalent stress and first principal stress for the octet lattice are presented in Fig. 22 and Fig. 23, respectively. The stress concentration occurs at the junction of several pillars and is higher in the middle of the specimen. As expected, the analysis of the first principal stress (Fig. 23) shows a dominant tensile stress in the whole specimen under a uniaxial tensile test.

4. Discussion

This study delves into the non-resistant layer and the internal porosity of nylon SLS printed lattices. The most important finding is that to obtain the mechanical properties, avoiding the effect of the geometry of the specimen, a double reduction of the diameter has been carried out. The final diameter after this double reduction considers only the effective cross section that can withstand stress. A fracture model based on the σ_{UTS} allows the material failure of lattice structures to be appropriately simulated based on the proposed methodology. In addition, using second order tetrahedra (10 nodes) elements for meshing the lattice, effects of stress concentration at pillar joints are modeled.

Although compressed air was used to clean all the specimens, bead blasting is usually more suitable to clean SLS printed parts. However, in lattices with a high number of small pillars, it is difficult to clean the internal ones as good as the external pillars. To correctly study how the diameter of designed pillars differs from printed ones, compressed air was selected to maintain constant all diameters of specimens and lattices. Regular lattices, such as FCC, BCC, and Octet, were used to validate the methodology. Stochastic lattices are not considered here, even though they are as common as regular lattices. When using stochastic lattices, pillars are likely to be printed in the Z axis of the printer [25]. Hence, to model their behavior in a FEM analysis, more complete knowledge of the material anisotropy is required. That, however, is out of the scope of the present paper. Nevertheless, a more profound study of

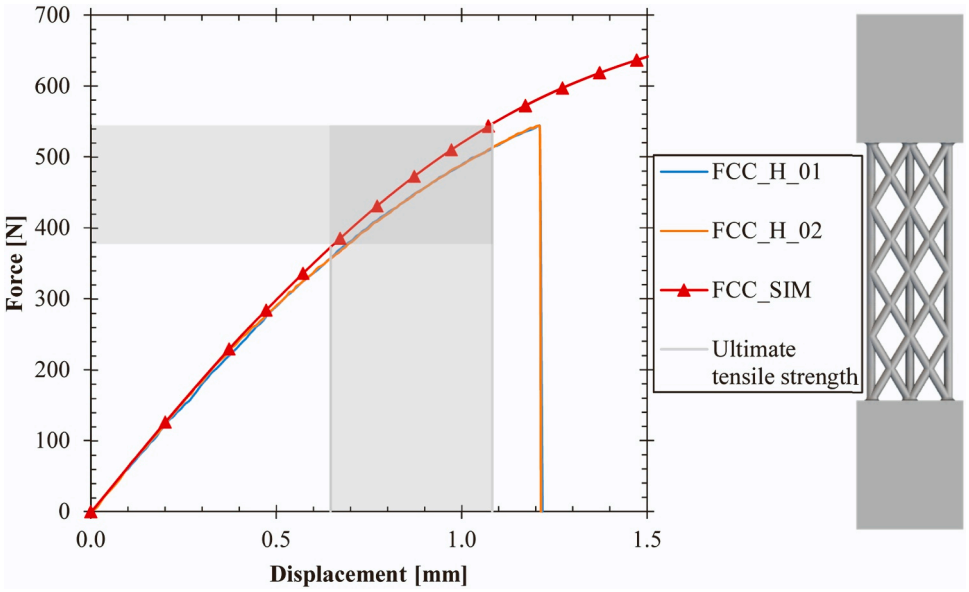

Fig. 20. FCC comparison between simulation with fracture limits and tests.

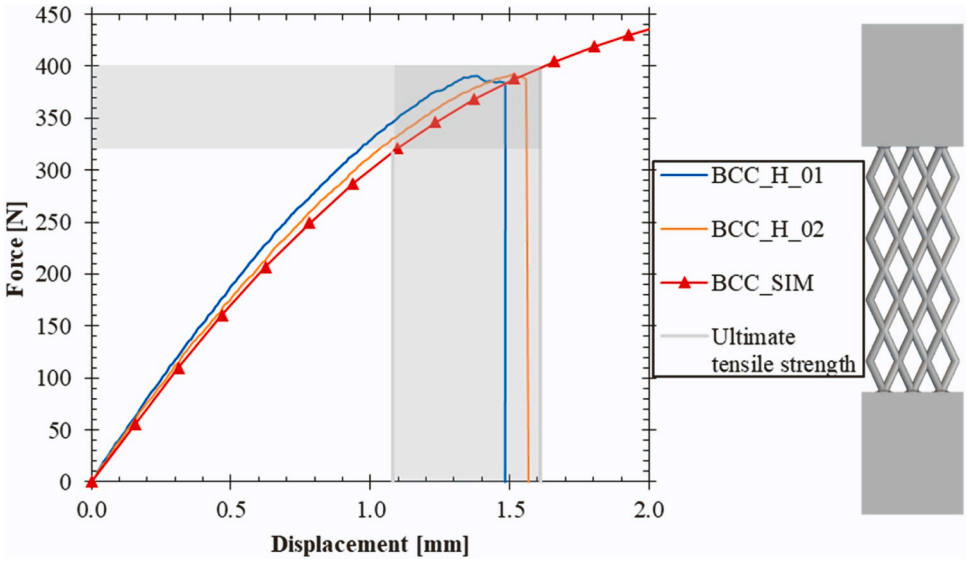

Fig. 21. BCC comparison between simulation with fracture limits and tests.

an adequate failure criterion could be beneficiary. Van Melick et al. [26] studied for other polymers that despite the application of different strain rates, the maximum hydrostatic stress is barely influenced. A similar failure criterion for PA-12 could be applied to the present methodology. The model of damage of Gurson-Tvergaard-Needleman (GTN) [20] could also be implemented to simulate the curve of the material until fracture.

The present methodology analyzes different flaw sizes on the macroscopic behavior of the specimen. In should be noted that analyzed defects are simplified by a disc-type flaw and do not consider the stress concentrating factor due to the radius of the notch or the irregularity of the geometry that may appear at the edge of the defect. In addition, porosity was estimated using a FEM analysis to correct the material properties without experimental comparison. Similar porosity is found on other studies [3,10], although it varies according to printer parameters. This is, nevertheless, a complex task, as the skin of the specimen needs to be eliminated first to avoid an analysis with external porosity. In addition, several measurements must be performed to obtain an average porosity.

This methodology allows to simulate through FEM the real behavior of PA-12 printed lattices with a good degree of accuracy regardless of pillar size. Moreover, it can be used to obtain and correct mechanical properties of standard tests on different printers considering the external layer and internal porosity.

5. Conclusion and future work

This study has presented a methodology to characterize the behavior of different size printed pillars, enabling to utilize the obtained properties from standard tensile testing to simulate with a good degree of accuracy parts with lattice structures printed with SLS technology.

The proposed methodology is based on two consecutive corrections. They permit to obtain an effective diameter, which takes into account the effect of defects and the influence of the diameter size of pillars in mechanical behavior.

The first proposed correction eliminates the badly adhered outer

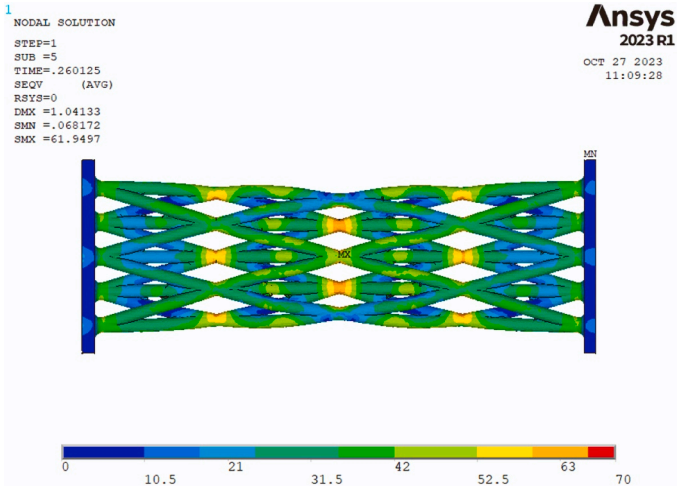

Fig. 22. Von-Mises equivalent stress in step 5 of the simulation of octet lattice.

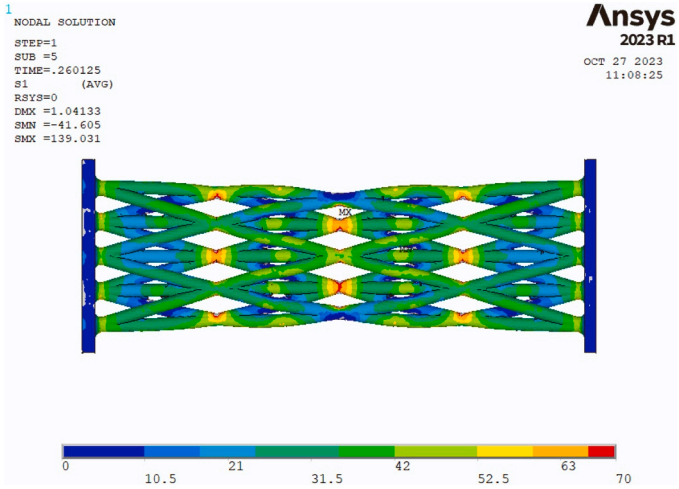

Fig. 23. First principal stress in step 5 of the simulation of octet lattice.

layer of powder, indicated as skin. This outer layer has poor properties in comparison with the fully melted material. As a consequence of this skin correction, the initial part of the stress-strain curves coincides.

The second correction takes into account the randomly distributed defects of fusion by introducing a porosity factor. These two corrections are always applied, both to obtain the mechanical behavior of the pure material and to obtain the effective diameter from the nominal diameter of the pillars. The final effective diameter ready to simulate with the corrected material is computationally less demanding and it is not necessary to include complex models of defects.

The fracture surface analysis shows that internal defects are stress concentrators. Near or surrounding these defects, the material starts to craze, i.e. small internal holes at micro scale appear that are followed by a whitening of the zone. Once the σ_{UTS} is reached in this zone, final brittle fracture occurs for the rest of the cross-section.

As a next step, the presented methodology could be extended by implementing a more advanced failure criterion. Also, the model can be extended to an anisotropic model, taking into account the differences in behavior in the horizontal and vertical directions (see Table 4).

CRediT authorship contribution statement

R. Rodríguez-Aparicio: Writing – original draft, Software, Methodology, Investigation, Data curation, Conceptualization. **J.M. Alegre:** Writing – review & editing, Supervision, Methodology, Investigation, Funding acquisition, Conceptualization. **W.M.H. Verbeeten:** Writing – review & editing, Supervision, Methodology, Investigation, Conceptualization. **M. Lorenzo-Bañuelos:** Investigation, Data curation. **I.I. Cuesta:** Writing – review & editing, Project administration, Investigation, Funding acquisition.

Declaration of Competing Interest

The authors declare that they have no known competing financial interests or personal relationships that could have appeared to influence the work reported in this paper.

Data availability

Data will be made available on request.

Acknowledgements

The authors wish to acknowledge the funding received through the Junta de Castilla y León projects BU-002-P20 and INVESTUN/22/BU/0003 co-financed with FEDER funds, and the projects MR5W.P3 (C17.I01. P01. S21) and MR4W.P2 co-financed by JCyL and MICINN and the NextGenerationEU/PRTR funds.

References

[1] R.D. Goodridge, C.J. Tuck, R.J.M. Hague, Laser sintering of polyamides and other polymers, Prog. Mater. Sci. 57 (2012) 229–267, https://doi.org/10.1016/j.pmatsci.2011.04.001.
[2] Z. Xu, Y. Wang, D. Wu, K.P. Ananth, J. Bai, The process and performance comparison of polyamide 12 manufactured by multi jet fusion and selective laser sintering, J. Manuf. Process 47 (2019) 419–426, https://doi.org/10.1016/j.jmapro.2019.07.014.
[3] A. Salazar, A. Rico, J. Rodríguez, J. Segurado Escudero, R. Seltzer, F. Martin De La Escalera Cutillas, Fatigue crack growth of SLS polyamide 12: Effect of reinforcement and temperature, Compos B Eng. 59 (2014) 285–292, https://doi.org/10.1016/j.compositesb.2013.12.017.
[4] A.A.M. Damanhuri, A. Hariri, S.A. Ghani, M.S.S. Mustafa, S.G. Herawan, N. A. Paiman, The effects of virgin and recycled PA12 powders in SLS processes on occupational exposures, Int. J. Environ. Sci. Dev. 12 (2021) 339–345, https://doi.org/10.18178/IJESD.2021.12.11.1359.
[5] C. Neff, N. Hopkinson, N.B. Crane, Experimental and analytical investigation of mechanical behavior of laser-sintered diamond-lattice structures, Addit. Manuf. 22 (2018) 807–816, https://doi.org/10.1016/j.addma.2018.07.005.
[6] F. Concli, A. Gilioli, Numerical and experimental assessment of the static behavior of 3D printed reticular Al structures produced by Selective Laser Melting: Progressive damage and failure. Procedia Structural Integrity, Elsevier B.V.,, 2018, pp. 204–212, https://doi.org/10.1016/j.prostr.2018.11.094.
[7] D.-I.. Gianpaolo Savio, Design method and taxonomy of optimized regular cellular structures for additive manufacturing technologies, in: Proceedings of the 20th International Conference on Engineering Design (ICED15), Milan, Italy, 2015.
[8] A. Salazar, A. Rico, J. Rodríguez, J. Segurado Escudero, R. Seltzer, F. Martin De La Escalera Cutillas, Monotonic loading and fatigue response of a bio-based polyamide PA11 and a petrol-based polyamide PA12 manufactured by selective laser sintering, Eur. Polym. J. 59 (2014) 36–45, https://doi.org/10.1016/j.eurpolymj.2014.07.016.
[9] A. Lindberg, J. Alfthan, H. Pettersson, G. Flodberg, L. Yang, Mechanical performance of polymer powder bed fused objects – FEM simulation and verification, Addit. Manuf. 24 (2018) 577–586, https://doi.org/10.1016/j.addma.2018.10.009.
[10] T. Stichel, T. Frick, T. Laumer, F. Tenner, T. Hausotte, M. Merklein, M. Schmidt, A Round Robin study for Selective Laser Sintering of polyamide 12: Microstructural origin of the mechanical properties, Opt. Laser Technol. 89 (2017) 31–40, https://doi.org/10.1016/j.optlastec.2016.09.042.
[11] N. Lammens, M. Kersemans, I. De Baere, W. Van Paepegem, On the visco-elasto-plastic response of additively manufactured polyamide-12 (PA-12) through selective laser sintering, Polym. Test. 57 (2017) 149–155, https://doi.org/10.1016/j.polymertesting.2016.11.032.
[12] M. Faes, Y. Wang, P. Lava, D. Moens, Variability, heterogeneity, and anisotropy in the quasi-static response of laser sintered PA12 components, Strain 53 (2017), e12219, https://doi.org/10.1111/str.12219.
[13] S. Dupin, O. Lame, C. Barrès, J.Y. Charmeau, Microstructural origin of physical and mechanical properties of polyamide 12 processed by laser sintering, Eur. Polym. J. 48 (2012) 1611–1621, https://doi.org/10.1016/j.eurpolymj.2012.06.007.
[14] A. El Magri, S.E. Bencaid, H.R. Vanaei, S. Vaudreuil, Effects of laser power and hatch orientation on final properties of PA12 parts produced by selective laser sintering, Polymers 14 (2022) 3674, https://doi.org/10.3390/polym14173674.

[15] D. Bruson, M. Galati, F. Calignano, L. Iuliano, Mechanical characterisation and simulation of the tensile behaviour of polymeric additively manufactured lattice structures, Exp. Mech. (2023), https://doi.org/10.1007/s11340-023-00976-5.
[16] B. Lozanovski, D. Downing, R. Tino, A. du Plessis, P. Tran, J. Jakeman, D. Shidid, C. Emmelmann, M. Qian, P. Choong, M. Brandt, M. Leary, Non-destructive simulation of node defects in additively manufactured lattice structures, Addit. Manuf. 36 (2020), https://doi.org/10.1016/j.addma.2020.101593.
[17] K.M. Park, K.S. Min, Y.S. Roh, Design optimization of lattice structures under compression: study of unit cell types and cell arrangements, Materials 15 (2022) 97, https://doi.org/10.3390/ma15010097.
[18] J. Plocher, V.L. Tagarielli, A. Panesar, Predictions of the elastic–plastic compressive response of functionally graded polymeric composite lattices manufactured by three-dimensional printing, J. Eng. Mater. Technol. 145 (2023), 011006, https://doi.org/10.1115/1.4055472.
[19] V.S. Deshpande, N.A. Fleck, Isotropic constitutive models for metallic foams, Mech. Phys. Solids 48 (2000) 1253–1283, https://doi.org/10.1016/S0022-5096(99)00082-4.
[20] D. Schob, R. Roszak, I. Sagradov, H. Sparr, M. Ziegenhorn, A. Kupsch, F. Léonard, B.R. Müller, G. Bruno, Experimental determination and numerical simulation of material and damage behaviour of 3D printed polyamide 12 under quasi-static loading, Arch. Mech. 71 (2019) 489–505, https://doi.org/10.24423/aom.3162.
[21] M. Smith, Z. Guan, W.J. Cantwell, Finite element modelling of the compressive response of lattice structures manufactured using the selective laser melting technique, Int J. Mech. Sci. 67 (2013) 28–41, https://doi.org/10.1016/j.ijmecsci.2012.12.004.
[22] S. Tsopanos, R.A.W. Mines, S. McKown, Y. Shen, W.J. Cantwell, W. Brooks, C. J. Sutcliffe, The influence of processing parameters on the mechanical properties of selectively laser melted stainless steel microlattice structures, J. Manuf. Sci. Eng. 132 (2010), 041011, https://doi.org/10.1115/1.4001743.
[23] S. Rosso, R. Meneghello, L. Biasetto, L. Grigolato, G. Concheri, G. Savio, In-depth comparison of polyamide 12 parts manufactured by Multi Jet Fusion and Selective Laser Sintering, Addit. Manuf. 36 (2020), 101713, https://doi.org/10.1016/j.addma.2020.101713.
[24] S. Gümüs, J.M. Lackner, Ş. Polat, W. Kraschitzer, H. Hanning, A. Bayram, M. Kaya, M. Çalll, A. Alkan, Failure behavior of PA12 based SLS lattice structure with macro-porosity, MATEC Web Conf. EDP Sci. (2018), https://doi.org/10.1051/matecconf/201818803007.
[25] D.A. Porter, M.A. Di Prima, Y. Badhe, A.R. Parikh, Nylon lattice design parameter effects on additively manufactured structural performance, J. Mech. Behav. Biomed. Mater. 125 (2022), https://doi.org/10.1016/j.jmbbm.2021.104869.
[26] H.G.H. Van Melick, O.F.J.T. Bressers, J.M.J. Den Toonder, L.E. Govaert, H.E. H. Meijer, A micro-indentation method for probing the craze-initiation stress in glassy polymers, Polymer 44 (2003) 2481–2491, https://doi.org/10.1016/S0032-3861(03)00110-1.